Neutron activation and prompt gamma intensity in Ar/CO$_2$-filled neutron detectors at the European Spallation Source

E. Dian[a,b,c,*], K. Kanaki[b], R. J. Hall-Wilton[b,d], P. Zagyvai[a,c], Sz. Czifrus[c]

[a]*Hungarian Academy of Sciences, Centre for Energy Research, 1525 Budapest 114., P.O. Box 49., Hungary*
[b]*European Spallation Source ESS ERIC, P.O Box 176, SE-221 00 Lund, Sweden*
[c]*Budapest University of Technology and Economics, Institute of Nuclear Techniques, 1111 Budapest, Műegyetem rakpart 9.*
[d]*Mid-Sweden University, SE-851 70 Sundsvall, Sweden*

Abstract

Monte Carlo simulations using MCNP6.1 were performed to study the effect of neutron activation in Ar/CO$_2$ neutron detector counting gas. A general MCNP model was built and validated with simple analytical calculations. Simulations and calculations agree that only the ^{40}Ar activation can have a considerable effect. It was shown that neither the prompt gamma intensity from the ^{40}Ar neutron capture nor the produced ^{41}Ar activity have an impact in terms of gamma dose rate around the detector and background level.

Keywords: ESS, neutron detector, B4C, neutron activation, ^{41}Ar, MCNP, Monte Carlo simulation

1. Introduction

Ar/CO$_2$ is a widely applied detector counting gas, with long history in radiation detection. Nowadays, the application of Ar/CO$_2$-filled detectors is extended in the field of neutron detection as well. However, the exposure of Ar/CO$_2$ counting gas to neutron radiation carries the risk of neutron activation. Therefore, detailed consideration of the effect and amount of neutron

---

*Corresponding author
Email address:* `dian.eszter@energia.mta.hu` (E. Dian)

induced radiation in the Ar/CO_2 counting gas is a key issue, especially for large volume detectors.

In this paper methodology and results of detailed analytical calculations and Monte Carlo simulations of prompt and decay gamma production in boron-carbide-based neutron detectors filled with Ar/CO_2 counting gas are presented (see Appendix).

In Section 2 a detailed calculations method for prompt gamma and activity production and signal-to-background ratio is introduced, as well as a model built in MCNP6.1 for the same purposes. The collected bibliographical data (cross section, decay constant) and the cross section libraries used for MCNP6.1 simulation are also presented.

In Section 3 the results of the analytical calculations and the simulation, their comparison and their detailed analysis are given.

In Section 4 the obtained results are concluded from the aspects of gamma emission during and after irradiation, radioactive waste production and emission, and the effect of self-induced gamma background on the measured signal.

2. Context

The European Spallation Source (ESS) has the goal to be the world's leading neutron source for the study of materials by the second quarter of this century [1; 2]. Large scale material-testing instruments, beyond the limits of the current state-of-the-art instruments are going to be served by the brightest neutron source in the world, delivering 5 MW power on target. At the same time the ^{3}He crisis instigates detector scientists to open a new frontier for potential ^{3}He substitute technologies and adapt them to the requirements of the large scale instruments that used to be fulfilled by well-tested ^{3}He detectors. One of the most promising replacements is the ^{10}B converter based gaseous detector technology, utilising an Ar/CO_2 counting gas. Ar/CO_2-filled detectors will be utilised among others for inelastic neutron spectrometers [3–6], where on the one hand, very large detector volumes are foreseen, on the other hand, very low background radiation

2

is required. Consequently, due to the high incoming neutron intensity and large detector volumes, the effects of neutron-induced reactions, especially neutron activation in the solid body or in the counting gas of the detector could scale up and become relevant, both in terms of background radiation and radiation safety.

Gaseous detectors. The gaseous ionisation chamber is one of the most common radiation detectors. The ionisation chamber itself is a gas filled tank that contains two electrodes with DC voltage [7; 8]. The detection method is based on the collision between atoms of the filling gas and the photons or charged particles to detect, during which electrons and positively charged ions are produced. Due to the electric field between the electrodes, the electrons drift to the anode, inducing a measurable signal. However, this measurable signal is very low, therefore typically additional are wires included and higher voltage is applied in order to obtain a gain on the signal, while the signal is still proportional to the energy of the measured particle; these are the so-called proportional chambers [9]. These detectors can be used as neutron detectors if appropriate converters are applied that absorb the neutron while emitting detectable particles via a nuclear reaction. In the case of ^{3}He- or ^{10}BF$_3$-based detectors the converter is the counting gas itself, but solid converters could be used as well with conventional counting gases.

Thermal neutron detector development. One leading development has been set on the Ar/CO$_2$ gas filled detectors with solid enriched boron-carbide (^{10}B$_4$C) neutron converters [10], detecting neutrons via the ^{10}B(n,α)^{7}Li reaction [11–14]. With this technology the optimal thickness of the boron-carbide layer is typically 1 μm [15], otherwise the emitted α particle is stopped inside the layer and remains undetected. But, a thinner boron-carbide layer means smaller neutron conversion efficiency. The idea behind the detector development at ESS is the multiplication of boron-carbide neutron converter layers by using repetitive geometrical structures, in order to increase the neutron conversion

3

efficiency and obtain a detection efficiency that is competitive with that of the ^{3}He detectors [11; 12].

Shielding issues in detector development. The modern neutron instruments are being developed to reach high efficiency, but also higher performance, such as time or energy resolution to open new frontiers in experimentation. One of the most representative characteristics of these instruments is the signal-to-background ratio, which is targeted in the optimisation process. While the traditional solutions for improving the signal-to-background ratio are based on increasing the source power and improving the transmittance of neutron guides, for modern instruments the background reduction via optimised shielding becomes equally relevant. For state-of-the-art instruments the cost of a background reducing shielding can be a major contribution in the total instrument budget [16]. In order to optimise the shielding not only for radiation safety purposes but in order to improve the signal-to-background ratio a detailed map of potential background sources is essential. While the components of the radiation background coming from the neutron source and the neutron guide system are well known, the effect of newly developed boron-carbide converter based gaseous detectors still has to be examined, especially the background radiation and potential self-radiation coming from the neutron activation of the solid detector components and of the detector filling gas.

Argon activation. The experience over the last decades showed that for facilities, e.g. nuclear power plants, research reactors and research facilities with accelerator tunnels, there is a permanent activity emission during normal operation that mainly contains airborne radionuclides [17–24]. For most of these facilities ^{41}Ar is one of the major contributors to the radiation release. ^{41}Ar is produced via thermal neutron capture from the naturally occurring ^{40}Ar, which is the main isotope of natural argon with 99.3 % abundance [25]. At most facilities ^{41}Ar is produced from the irradiation of the natural argon content of air. In air-cooled and water-cooled reactors ^{40}Ar is exposed in the reactor core as part of the coolant; in the latter case it is coming from the air dissolved

in the primary cooling water. Air containing argon is also present in the narrow gap between the reactor vessel and the biological shielding. The produced ^{41}Ar mixes with the air of the reactor hall and is removed by the ventilation system. In other facilities ^{41}Ar is produced in the accelerator tunnel. In all cases, within the radiation safety plan of the facility the ^{41}Ar release is taken into account [26] and well estimated either via simple analytical calculations or Monte Carlo simulations. The average yearly ^{41}Ar release of these facilities can reach a few thousand GBq.

For the ESS the ^{41}Ar release coming from the accelerator and the spallation target is already calculated [27–29], but in addition the exposure of the large volume of Ar/CO_2 contained in the neutron detectors should also be considered. Due to the 70-90 % argon content of the counting gas and the fact that most instruments operate with thermal or cold neutron flux that leads to a higher average reaction rate, the ^{41}Ar production in the detectors could be commensurate with the other sources. For all the above mentioned reasons, argon activation is an issue to consider at ESS both in terms of activity release and in terms of occupational exposure in the measurement hall.

3. Applied methods

Analytical calculation for neutron activation. Neutron activation occurs during the (n,γ) reaction where a neutron is captured by a target nucleus. The capture itself is usually followed by an instant photon emission; these are the so called prompt photons. The energies of the emitted prompt photons are specific for the target nucleus. After capturing the neutron, in most cases the nucleus gets excited, and becomes radioactive; this is the process of neutron activation, and the new radionuclide will suffer decay with its natural half-life. Due to their higher number of neutrons, the activated radionuclei mostly undergo β^- decay, accompanied by a well-measurable decay gamma radiation. The gamma energies are specific for the radionucleus. These two phenomena form the basics of two long-used and reliable analytical techniques, the neutron activation anal-

ysis (NAA [30–32]) and the prompt gamma activation analysis (PGAA [33]). Consequently, detailed measured and simulated data are available for neutron activation calculation.

For shielding and radiation safety purposes the produced activity concentration (a [Bq/cm^3]) and the prompt photon intensity have to be calculated that are depending on the number of activated nuclei (N^* [1/cm^3]). The production of radionuclides (*reaction rate*) depends on the number of target nuclei (N_0 [1/cm^3]) for each relevant isotope, the irradiating neutron flux (Φ [n/cm^3/s]) and the (n,γ) reaction cross section (σ [cm^2]) at the irradiating neutron energies, while the loss of radionuclides is determined by their decay constants (λ [1/s]). A basic assumption is that the number of target nuclei can be treated as constant if the loss of target nuclei during the whole irradiation does not exceed 0.1 %. This condition is generally fulfilled, like in the cases examined in this study, therefore the rate of change of the number of activated nuclei is given by Equation 1.

$$\frac{dN^*}{dt} = N_0 \cdot \Phi \cdot \sigma - \lambda \cdot N^* \tag{1}$$

With the same conditions, the activity concentration after a certain time of irradiation ($t_{irr}[s]$) can be calculated with Equation 2.

$$a\left(t_{irr}\right) = N_0 \cdot \Phi \cdot \sigma \cdot \left(1 - e^{\lambda t_{irr}}\right) \tag{2}$$

In this study, as the activation calculation is based on Equation 2, the activity yield of the naturally present radionuclides (e.g. cosmogenic ^{14}C in CO_2) is ignored due to the very low abundance of these nuclides. The activity yield of the secondary activation products, the products of multiple independent neutron captures on the same target nucleus, are ignored as well, because of the low probability of the multiple interaction.

The prompt gamma intensity (I [1/s/cm^3]) coming from the neutron capture can be calculated similarly to the (n,γ) reaction rate. In this case a prompt gamma line (i) specific cross section ($\sigma_{pg,i}$) has to be used [34], that is proportional to the (n,γ) cross section, the natural abundance of the target isotope in

the target element, and the weight of the specific gamma energy with respect to the total number of gamma lines. For this reason in Equation 3 the number of target nuclei corresponds to the element (N_0' [1/cm^3]), not the isotope (N_0 [1/cm^3]).

$$I_i = N_0' \cdot \Phi \cdot \sigma_{pg,i} \tag{3}$$

In the current study, activity concentration, prompt gamma intensity and the respective prompt gamma spectrum have been calculated for each isotope in the natural composition [25] of an 80/20 volume ratio Ar/CO_2 counting gas at room temperature and 1 bar pressure and in an aluminium alloy used for the detector frame. Alloy Al5754 [35] has been chosen as a typical alloy used in nuclear science for mechanical structures. Activity concentration and prompt gamma intensity calculations have been done for several monoenergetic neutron beams in the range of 0.6–10 Å (227.23–0.82 meV). Since for isotopes of interest the energy dependence of the (n,γ) cross section is in the 1/v (velocity) region [36; 37], the cross sections for each relevant energy have been easily extrapolated from the thermal (1.8 Å) neutron capture cross sections listed in Table A1.

The irradiating neutron flux has been approximated with 10^4 n/cm^2/s. This value has been determined for a worst case scenario based on the following assumptions: the planned instruments are going to have various neutron fluxes at the sample position, and the highest occurring flux can be conservatively estimated to 10^{10} n/cm^2/s [38]. The neutron fraction scattered from the sample is in the range of 1-10 %. Calculating with 10 %, the approximation remains conservative. A realistic sample surface is 1 cm^2, reducing the scattered flux to 10^9 n/s. The sample-detector distance also varies among the instruments, so the smallest realistic distance of 100 cm was used for a conservative approximation. Therefore the neutron yield has to be normalised to a 10^5 cm^2 surface area at this sample-detector distance. According to these calculations, 10^4 n/cm^2/s is a conservative estimation for the neutron flux the detector is exposed to.

This simple approach allows that the result can be scaled to alternate input conditions, i.e. a higher neutron flux or detector geometry.

MCNP simulation for neutron activation. Monte Carlo simulations have been performed in order to determine the expected activity concentration and prompt gamma intensity in the counting gas and the aluminium frame of boron-carbide-based neutron detectors.

The MCNP6.1 [39] version has been used for the simulations. The detector gas volume has been approximated as a generic 10 cm x 10 cm x 10 cm cube, surrounded by a 5 mm thick aluminium box made of Al5754 alloy, representing the detector frame, as it is described in Figure 1. In order to avoid interference with the prompt photon emission of the Ar/CO_2, the counting gas was replaced with vacuum while observing the activation on the aluminium frame. The detector geometry has been irradiated with a monoenergetic neutron beam from a monodirectional disk source of 8.5 cm radius at 50 cm distance from the surface of the target volume. A virtual sphere has been defined around the target gas volume with 10 cm radius for simplifying prompt photon counting. Both the activity concentration and the prompt gamma intensity determined with MCNP6.1 simulations have been scaled to a 10^4 n/cm^2/s irradiating neutron flux.
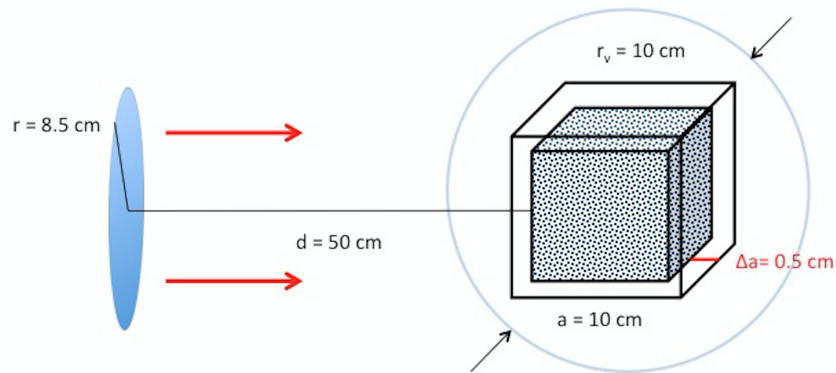

Figure 1: Neutron irradiation geometry used in MCNP6 simulation.

Different runs have been prepared for each element in the gas mixture and the Al5754 alloy to determine the prompt gamma spectrum and total intensity. The prompt photon spectrum has been determined for each element with the following method: a virtual sphere has been defined around the cubic target volume. Since the target volume was located in vacuum, all the prompt photons produced in a neutron activation reaction have to cross this virtual surface. Within MCNP, the particle current integrated over a surface, can be easily determined (F1 tally [39]). Knowing the volume of the target, the prompt photon intensity can be calculated for the simulated neutron flux (Φ_{MCNP}, [flux/source particle]). After the Φ_{MCNP} average neutron flux in the target volume has been determined (F4 tally [39]), the prompt photon intensity can be scaled for any desired neutron flux, 10^4 n/cm^2/s in this case. With this method the self-absorption of the target gas volume can be considered to be negligible.

The activity concentration is not given directly by the simulation, but it can be calculated from the R_{MCNP} reaction rate (reaction/source particle) and the Φ_{MCNP} flux. The R_{MCNP} is calculated in MCNP in the following way: first the track length density of neutrons has to be determined in the target volume (F4 tally [39]), and then this value has to be multiplied with the reaction cross section of the specific reaction of interest, through the entire spectrum, taking into account the number of target nuclei of the irradiated material (FM tally multiplication card [39]). In the current simulations each isotope has been defined as a different material, with their real partial atomic density ([atom/barn/cm]) in the counting gas or in the aluminium alloy for the (n,γ) reaction (ENDF reaction 102). As the reaction rate given by the MCNP simulation is the saturated reaction rate for the Φ_{MCNP} flux, and contains all the geometrical and material conditions of the irradiation, the time-dependent activity concentration for any Φ flux can be calculated with Equation 4.

$$a\left(t_{irr}\right) = R_{MCNP} \cdot \frac{\Phi}{\Phi_{MCNP}} \cdot \left(1 - e^{\lambda t_{irr}}\right) \tag{4}$$

9

In order to determine the above mentioned quantities, the cross section libraries have to be chosen carefully for the simulation. Within the current study different libraries have been used to simulate the prompt gamma production and the reaction rates. Several databases have been tested, but only a few of them contain data on photon production for the isotopes of interest. Tables A2 and A4 present the combinations that give the best agreement with the theoretical expectations, especially in terms of spectral distribution. These are the ENDF [37], TALYS [40] and LANL [41] databases.

The MCNP6.1 simulation has been repeated for each naturally occurring isotope in the counting gas and the aluminium frame, and analytical calculations have been also prepared to validate the simulation, in order to obtain reliable and well-applicable data on the detector housing and counting gas activation and gamma emission both for shielding and for radiation protection purposes.

In order to demonstrate the effect of gamma radiation on the measured signal, the signal-to-background has been calculated for a typical and realistic detector geometry. A generic boron-carbide based detector can be represented by a 5-20 mm thick gas volume surrounded by a few millimetre thin aluminium box, carrying the few micrometers thick boron-carbide converter layer(s). The gas volume is determined by the typical distance needed for the energy deposition. In a realistic application, a larger gas volume used to be used for efficiency purposes, built up from the above mentioned subvolumes. As a representative example a $V_{gas} = 256\ cm^3$ counting gas volume has been chosen as the source of gamma production, with an $A_{in} = 16\ cm^2$ entrance surface for incident neutrons, divided into 20 mm thick subvolumes by 16 layers of 2 μm thin enriched boron-carbide.

In this study the gamma efficiency has been approximated with 10^{-7} for the entire gamma energy range [42; 43] due to its relatively low energy-dependence, whereas the neutron efficiency has been calculated for all the mentioned energies on the basis of [11], resulting in a neutron efficiency varying between 0.4-0.72 within the given energy range. Therefore the measured signal and the signal of the gamma background were calculated as in Equations 5-6, where η_i is the

10

detection efficiency for the particle type i, Φ is the incident neutron flux and I_{photon} is the produced photon production in a unit gas volume. Signal-to-(gamma-)background ratio has been calculated as $S_n/S\gamma$.

$$S_n = A_{in} \cdot \Phi \cdot \eta_n \tag{5}$$

$$S_\gamma = V_{gas} \cdot I_{photon} \cdot \eta_\gamma \tag{6}$$

All calculations and simulations have been done for a 10^4 n/cm^2/s monoenergetic neutron irradiation for 0.6, 1, 1.8, 2, 4, 5 and 10 Å neutron wavelengths. Activity concentration has been calculated for $t_{irr} = 10^6$ s irradiation time and $t_{cool} = 10^7$ s cooling time. This irradiation time roughly corresponds to typical lengths of operation cycles for spallation facilities. Photon production has been normalised for a 1 cm^3 volume, irradiated with $\Phi = 1$ n/cm^2/s or $\Phi = 10^4$ n/cm^2/s neutron flux. Therefore here the photon production in a unit gas or aluminium volume irradiated with a unit flux is given as $\frac{\text{photon/cm}^3/\text{s}}{\text{n/cm}^2/\text{s}}$.

The uncertainties of the simulated and the bibliographical data have been taken into account. The MCNP6.1 simulations had high enough statistics, that the uncertainties of the simulated results were comparable to the uncertainties of the measured/bibliographical qualities used for the analytical calculations. The uncertainty of the total prompt photon production for all elements were below 5 % for the entire neutron energy range, while the uncertainties of the main prompt gamma lines were below 10 % for all elements, and less than 5 % for argon and the elements of the aluminium alloy.

For the anaytical calculations, the error propagation takes into account the uncertainty of the prompt gamma line specific cross section, given in the IAEA PGAA Database [34], being below 5 % for the main lines of all major isotopes, the σ absorption cross section and the λ decay constant (see Appendix). The obtained uncertainties of the photon intensities are generally within the size of the marker, here the error bars have been omitted. They have also been omitted for some of the spectra for better visibility.

11

4. Results and discussion

4.1. Prompt gamma intensity in detector counting gas

The total prompt photon production and its spectral distribution in Ar/CO_2 counting gas has been analytically calculated (Equation 3) on the basis of detailed prompt gamma data from IAEA PGAA Data-base [34]. The same data have been obtained with Monte Carlo simulation using MCNP6.1.

Prompt photon production normalised to incident neutron flux has been calculated for all mentioned wavelengths. The comparison of the result has shown, that the simulated and calculated total prompt photon yields qualitatively agree for Ar, C, and O within 2 %, 11 % and 21 %, respectively.
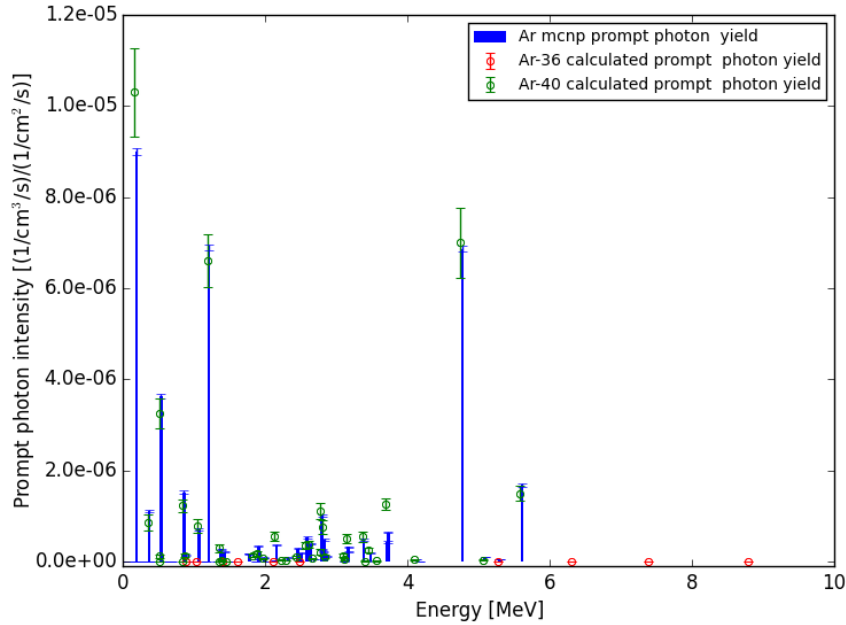

Figure 2: Prompt photon emission spectra from Ar in Ar/CO_2, irradiated with unit flux of 1.8 Å neutrons. Results of analytical calculation with input data taken from IAEA PGAA Database [34] and MCNP6.1 simulation, as explained in text. (For interpretation of the references to color in this figure caption, the reader is referred to the web version of this article.)

It has also been show that for these three elements proper cross section libraries can be found (see Table A2), the use of which in MCNP simulations produce prompt photon spectra that qualitatively agree with the calculated ones. As an example Figure 2 shows the simulated and calculated prompt photon spectra from argon in Ar/CO_2 for a 1.8 Å, $\Phi = 1$ n/cm^2/s neutron flux, irradiating a 1 cm^3 volume. Since numerous databases lack proper prompt photon data, this agreement is not trivial to achieve for all the elements. For these three elements MCNP simulations can effectively replace analytical calculations, which is especially valuable for more complex geometries. For all these reasons hereinafter only the MCNP6.1 simulated results are presented.
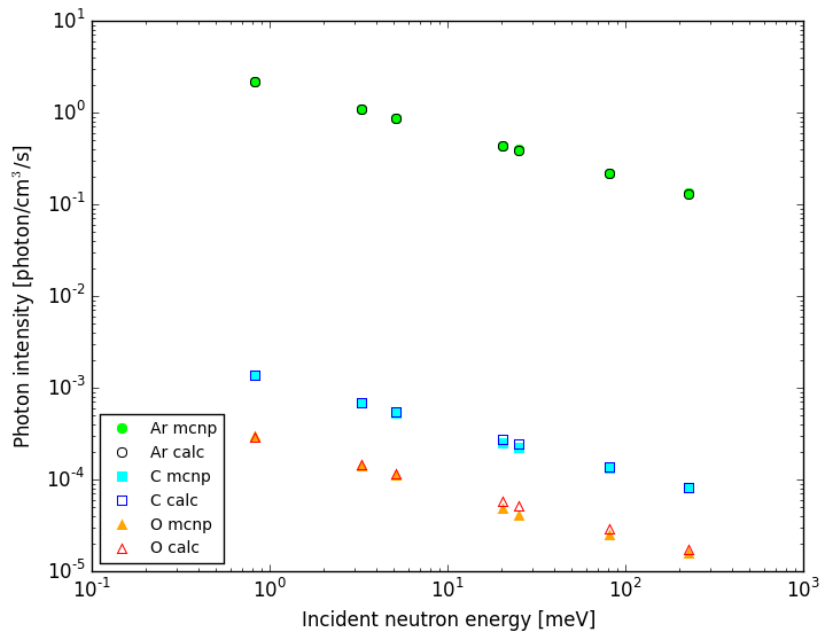

Figure 3: Elemental distribution of total prompt photon intensity in Ar/CO_2 counting gas irradiated with 10^4 n/cm^2/s neutron flux. Results of MCNP6.1 simulation and analytical calculations with input data taken from IAEA PGAA Database [34], as explained in text. (For interpretation of the references to color in this figure caption, the reader is referred to the web version of this article.)

In Figure 3 it is also shown, that the prompt photon emission is dominated

by argon, as expected due to the very small capture cross section of the oxygen and the carbon; the argon total prompt photon yield is 3 orders of magnitude higher than the highest of the rest. According to Figure 2, within the argon prompt gamma spectrum, there are 3 main gamma lines that are responsible for the majority of the emission; the ones at 167 ± 20 keV, 1187 ± 3 keV and 4745 ± 8 keV.

4.2. Activity concentration and decay gammas in detector counting gas

The induced activity in the irradiated Ar/CO_2 gas volume, as well as the photon yield coming from the activated radionuclei has been determined via analytical calculation, based on the bibliographical thermal (25.30 meV) neutron capture cross sections and the half-lives of the isotopes in the counting gas (see Table A1). A similar calculation has been prepared on the bases of reaction rates determined with MCNP simulations for each isotope of the counting gas. Activity concentrations obtained from the calculation and the MCNP6.1 simulation agree within the margin of error, therefore only the MCNP simulations are presented.

As an example the build-up of activity during irradiation time for 1.8 Å is given in Figure 4 for all the produced radionuclei.

It can be stated, that the total activity of the irradiated counting gas practically equals the ^{41}Ar activity (see Figure 4), which is $1.28 \cdot 10^{-1}$ Bq/cm^3 at the end of the irradiation time. This is 2 orders of magnitude higher than the activity of ^{37}Ar, which is $6.90 \cdot 10^{-4}$ Bq/cm^3, and 7 orders of magnitude higher than the activity of ^{38}Ar ($7.99 \cdot 10^{-9}$ Bq/cm^3) and ^{19}O ($3.19 \cdot 10^{-8}$ Bq/cm^3). The activity of carbon is negligible.

The decrease of activity in the detector counting gas because of the natural radioactive decay is shown in Figure 5. After the end of the irradiation the main component of the total activity is the ^{41}Ar, although it practically disappears after a day (10^5 s), due to its short 109.34 m half-life with ^{37}Ar becoming the dominant isotope. However, in terms of gamma emission, all the remaining isotopes, ^{37}Ar, ^{39}Ar and ^{14}C are irrelevant, since they are pure beta-emitters.
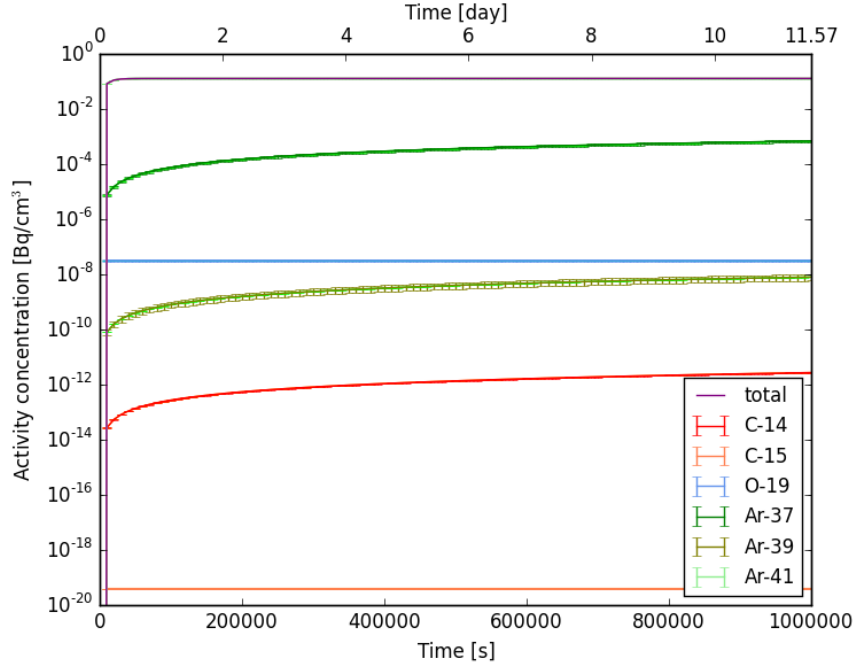
14

Figure 4: Build-up of isotopic and total activity concentration $[Bq/cm^3]$ in Ar/CO_2 during 10^6 s irradiation time. Results of MCNP6.1 simulation, as explained in text. (For interpretation of the references to color in this figure caption, the reader is referred to the web version of this article.)

Therefore, with the above listed conditions there is only minimal gamma emission from the Ar/CO_2 counting gas after 10^5 s cooling time. For the same reason, the ^{41}Ar activity quickly saturates and accordingly it can contribute to the gamma emission during the irradiation as well.

Decay gamma emission of the activated radionuclei from a unit volume per second, with the activity reached by the end of the irradiation time have been calculated. It is shown that the decay gamma yield practically all comes from the activated argon; the emission of the 1293.587 keV ^{41}Ar line is 8 orders of magnitudes higher than the yield of any other isotope.

Comparing the prompt and the maximum decay gamma emission of all the isotopes, as it is shown in Table 1, it is revealed that for the argon, the prompt
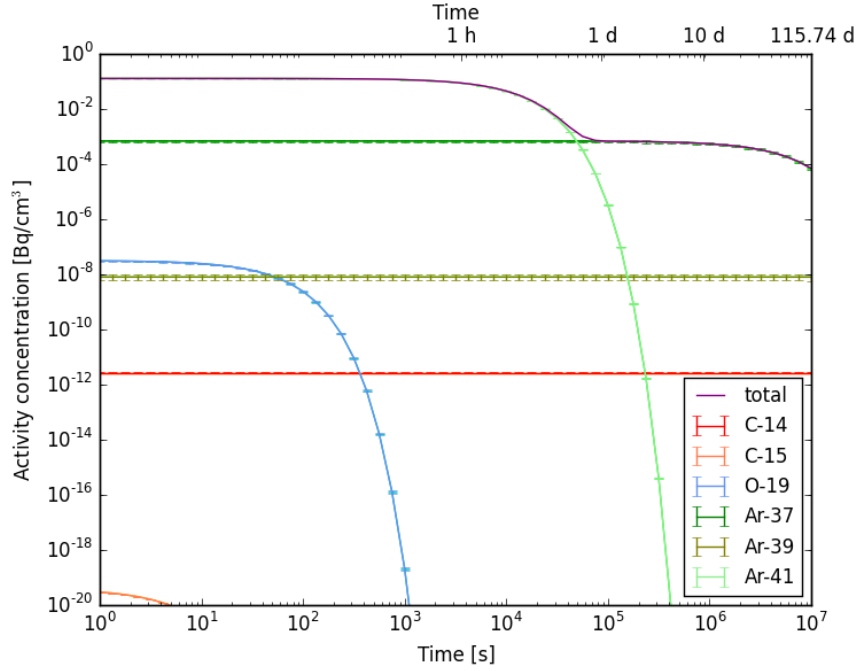
15

Figure 5: Decrease of activity concentration $[Bq/cm^3]$ in Ar/CO_2 from end of the 10^6 s irradiation period. Results of MCNP6.1 simulation, as explained in text. (For interpretation of the references to color in this figure caption, the reader is referred to the web version of this article.)

photon production $(3.9 \cdot 10^{-1} \frac{photon/cm^3/s}{n/cm^2/s})$ and the saturated decay gamma production $(1.27 \cdot 10^{-1} \frac{photon/cm^3/s}{n/cm^2/s})$ are comparable. There is a factor of 3 difference, whereas for carbon and oxygen the decay gamma production is negligible comparing with the prompt gamma production.

Figure 3 and Table 1 demonstrate that, as both the prompt and the decay gamma yield are determined by the neutron absorption cross section, their energy dependence follows the $1/v$ rule within the observed energy range in case of all the isotopes of the Ar/CO_2 counting gas. Therefore activation with cold neutrons produces a higher yield, and the thermal fraction is negligible.

As it has been indicated, most of the activated nuclei are beta emitters, and some of the isotopes in the Ar/CO_2 are pure beta emitters, therefore the

Table 1: Prompt and decay gamma emission from 80/20 V% Ar/CO_2 at 1 bar pressure and from Al5754 aluminium alloy, irradiated with 10^4 $\frac{1}{cm^2\,s}$ monoenergetic neutron flux for 10^6 s irradiation time. Results of MCNP6.1 simulation.

Element	Photon yield $\left[\frac{1}{cm^3 s}\right]$	Neutron wavelength [Å]						
		0.6	1	1.8	2	4	5	10
Ar	prompt	$1.32 \pm 0.04 \cdot 10^{-1}$	$2.15 \pm 0.05 \cdot 10^{-1}$	$3.96 \pm 0.08 \cdot 10^{-1}$	$4.37 \pm 0.09 \cdot 10^{-1}$	$8.64 \pm 0.14 \cdot 10^{-1}$	$1.080 \pm 0.016 \cdot 10^{0}$	$2.150 \pm 0.025 \cdot 10^{0}$
	decay	$4.227 \pm 0.001 \cdot 10^{-2}$	$7.045 \pm 0.002 \cdot 10^{-2}$	$1.2667 \pm 0.0003 \cdot 10^{-1}$	$1.4090 \pm 0.0004 \cdot 10^{-1}$	$2.8179 \pm 0.0007 \cdot 10^{-1}$	$3.5224 \pm 0.0009 \cdot 10^{-1}$	$7.044 \pm 0.002 \cdot 10^{-1}$
C	prompt	$8.1 \pm 1.4 \cdot 10^{-5}$	$1.33 \pm 0.18 \cdot 10^{-4}$	$2.21 \pm 0.23 \cdot 10^{-4}$	$2.51 \pm 0.25 \cdot 10^{-4}$	$5.33 \pm 0.36 \cdot 10^{-4}$	$6.9 \pm 0.4 \cdot 10^{-4}$	$1.36 \pm 0.06 \cdot 10^{-3}$
	decay	$8.49 \pm 0.11 \cdot 10^{-21}$	$1.44 \pm 0.02 \cdot 10^{-20}$	$2.51 \pm 0.03 \cdot 10^{-20}$	$2.79 \pm 0.04 \cdot 10^{-20}$	$5.56 \pm 0.07 \cdot 10^{-20}$	$6.94 \pm 0.09 \cdot 10^{-20}$	$1.39 \pm 0.02 \cdot 10^{-19}$
O	prompt	$1.58 \pm 0.43 \cdot 10^{-5}$	$2.51 \pm 0.55 \cdot 10^{-5}$	$4.1 \pm 0.7 \cdot 10^{-5}$	$4.81 \pm 0.77 \cdot 10^{-5}$	$1.12 \pm 0.12 \cdot 10^{-4}$	$1.43 \pm 0.14 \cdot 10^{-4}$	$2.96 \pm 0.19 \cdot 10^{-4}$
	decay	$1.619 \pm 0.035 \cdot 10^{-8}$	$2.70 \pm 0.06 \cdot 10^{-8}$	$4.8 \pm 0.1 \cdot 10^{-8}$	$5.40 \pm 0.12 \cdot 10^{-8}$	$1.08 \pm 0.02 \cdot 10^{-7}$	$1.35 \pm 0.03 \cdot 10^{-7}$	$2.69 \pm 0.06 \cdot 10^{-7}$
Al	prompt	$8.27 \pm 0.11 \cdot 10^{1}$	$1.379 \pm 0.015 \cdot 10^{2}$	$2.47 \pm 0.02 \cdot 10^{2}$	$2.75 \pm 0.02 \cdot 10^{2}$	$5.44 \pm 0.03 \cdot 10^{2}$	$6.76 \pm 0.03 \cdot 10^{2}$	$1.300 \pm 0.005 \cdot 10^{3}$
	decay	$4.4419 \pm 0.0018 \cdot 10^{1}$	$7.401 \pm 0.003 \cdot 10^{1}$	$1.3288 \pm 0.0005 \cdot 10^{2}$	$1.4773 \pm 0.0006 \cdot 10^{2}$	$2.929 \pm 0.001 \cdot 10^{2}$	$3.6373 \pm 0.0015 \cdot 10^{2}$	$6.9981 \pm 0.0028 \cdot 10^{2}$
Cr	prompt	$2.0 \pm 0.1 \cdot 10^{0}$	$3.35 \pm 0.14 \cdot 10^{0}$	$6.0 \pm 0.2 \cdot 10^{0}$	$6.7 \pm 0.2 \cdot 10^{0}$	$1.34 \pm 0.03 \cdot 10^{1}$	$1.680 \pm 0.036 \cdot 10^{1}$	$3.35 \pm 0.05 \cdot 10^{1}$
	decay	$5.4774 \pm 0.0026 \cdot 10^{-3}$	$9.131 \pm 0.004 \cdot 10^{-3}$	$1.6418 \pm 0.0008 \cdot 10^{-2}$	$1.8263 \pm 0.0009 \cdot 10^{-2}$	$3.653 \pm 0.002 \cdot 10^{-2}$	$4.566 \pm 0.002 \cdot 10^{-2}$	$9.130 \pm 0.004 \cdot 10^{-2}$
Cu	prompt	$7.3 \pm 0.1 \cdot 10^{-1}$	$1.23 \pm 0.13 \cdot 10^{0}$	$2.20 \pm 0.17 \cdot 10^{0}$	$2.44 \pm 0.19 \cdot 10^{0}$	$4.88 \pm 0.29 \cdot 10^{0}$	$6.09 \pm 0.34 \cdot 10^{0}$	$1.22 \pm 0.05 \cdot 10^{1}$
	decay	$6.44 \pm 0.03 \cdot 10^{-3}$	$1.073 \pm 0.005 \cdot 10^{-2}$	$1.93 \pm 0.01 \cdot 10^{-2}$	$2.15 \pm 0.01 \cdot 10^{-2}$	$4.29 \pm 0.02 \cdot 10^{-2}$	$5.366 \pm 0.026 \cdot 10^{-2}$	$1.073 \pm 0.005 \cdot 10^{-1}$
Fe	prompt	$1.69 \pm 0.12 \cdot 10^{0}$	$2.84 \pm 0.16 \cdot 10^{0}$	$5.1 \pm 0.2 \cdot 10^{0}$	$5.7 \pm 0.2 \cdot 10^{0}$	$1.13 \pm 0.03 \cdot 10^{1}$	$1.412 \pm 0.037 \cdot 10^{1}$	$2.82 \pm 0.05 \cdot 10^{1}$
	decay	$2.34 \pm 0.06 \cdot 10^{-4}$	$3.9 \pm 0.1 \cdot 10^{-4}$	$7.0 \pm 0.2 \cdot 10^{-4}$	$7.80 \pm 0.21 \cdot 10^{-4}$	$1.56 \pm 0.04 \cdot 10^{-3}$	$1.95 \pm 0.05 \cdot 10^{-3}$	$3.9 \pm 0.1 \cdot 10^{-3}$
Mg	prompt	$1.61 \pm 0.12 \cdot 10^{0}$	$2.68 \pm 0.17 \cdot 10^{0}$	$4.84 \pm 0.23 \cdot 10^{0}$	$5.38 \pm 0.24 \cdot 10^{0}$	$1.08 \pm 0.03 \cdot 10^{1}$	$1.345 \pm 0.038 \cdot 10^{1}$	$2.67 \pm 0.05 \cdot 10^{1}$
	decay	$3.19 \pm 0.03 \cdot 10^{-2}$	$5.32 \pm 0.05 \cdot 10^{-2}$	$9.56 \pm 0.09 \cdot 10^{-2}$	$1.06 \pm 0.01 \cdot 10^{-1}$	$2.12 \pm 0.02 \cdot 10^{-1}$	$2.652 \pm 0.025 \cdot 10^{-1}$	$5.279 \pm 0.049 \cdot 10^{-1}$
Mn	prompt	$1.77 \pm 0.06 \cdot 10^{1}$	$2.95 \pm 0.08 \cdot 10^{1}$	$5.30 \pm 0.11 \cdot 10^{1}$	$5.89 \pm 0.12 \cdot 10^{1}$	$1.18 \pm 0.02 \cdot 10^{2}$	$1.48 \pm 0.02 \cdot 10^{2}$	$2.95 \pm 0.03 \cdot 10^{2}$
	decay	$9.3 \pm 0.1 \cdot 10^{0}$	$1.56 \pm 0.02 \cdot 10^{1}$	$2.80 \pm 0.03 \cdot 10^{1}$	$3.114 \pm 0.036 \cdot 10^{1}$	$6.23 \pm 0.07 \cdot 10^{1}$	$7.79 \pm 0.09 \cdot 10^{1}$	$1.56 \pm 0.02 \cdot 10^{2}$
Si	prompt	$2.75 \pm 0.18 \cdot 10^{-1}$	$4.52 \pm 0.23 \cdot 10^{-1}$	$8.1 \pm 0.3 \cdot 10^{-1}$	$9.1 \pm 0.3 \cdot 10^{-1}$	$1.815 \pm 0.046 \cdot 10^{0}$	$2.27 \pm 0.05 \cdot 10^{0}$	$4.55 \pm 0.07 \cdot 10^{0}$
	decay	$1.6812 \pm 0.0007 \cdot 10^{-6}$	$2.802 \pm 0.001 \cdot 10^{-6}$	$5.038 \pm 0.002 \cdot 10^{-6}$	$5.604 \pm 0.002 \cdot 10^{-6}$	$1.1207 \pm 0.0004 \cdot 10^{-5}$	$1.4008 \pm 0.0006 \cdot 10^{-5}$	$2.801 \pm 0.001 \cdot 10^{-5}$
Ti	prompt	$2.60 \pm 0.15 \cdot 10^{0}$	$4.4 \pm 0.2 \cdot 10^{0}$	$7.8 \pm 0.3 \cdot 10^{0}$	$8.70 \pm 0.35 \cdot 10^{0}$	$1.75 \pm 0.05 \cdot 10^{1}$	$2.18 \pm 0.06 \cdot 10^{1}$	$4.36 \pm 0.09 \cdot 10^{1}$
	decay	$1.595 \pm 0.008 \cdot 10^{-3}$	$2.66 \pm 0.01 \cdot 10^{-3}$	$4.779 \pm 0.025 \cdot 10^{-3}$	$5.316 \pm 0.028 \cdot 10^{-3}$	$1.063 \pm 0.006 \cdot 10^{-2}$	$1.329 \pm 0.007 \cdot 10^{-2}$	$2.66 \pm 0.01 \cdot 10^{-2}$
Zn	prompt	$4.93 \pm 1.38 \cdot 10^{-1}$	$8.3 \pm 1.9 \cdot 10^{-1}$	$1.49 \pm 0.27 \cdot 10^{0}$	$1.66 \pm 0.29 \cdot 10^{0}$	$3.32 \pm 0.43 \cdot 10^{0}$	$4.13 \pm 0.48 \cdot 10^{0}$	$8.3 \pm 0.7 \cdot 10^{0}$
	decay	$1.114 \pm 0.008 \cdot 10^{-3}$	$1.86 \pm 0.01 \cdot 10^{-3}$	$3.338 \pm 0.025 \cdot 10^{-3}$	$3.71 \pm 0.03 \cdot 10^{-3}$	$7.42 \pm 0.06 \cdot 10^{-3}$	$9.28 \pm 0.07 \cdot 10^{-3}$	$1.86 \pm 0.01 \cdot 10^{-2}$

Table 2: Major endpoint energies and reaction energies of the main beta-emitters in Ar/CO_2 and in aluminium alloy Al5754 [25].

Isotope	Reaction product	Q_β [keV]	E_β [keV]	abundance	E_γ [keV]	abundance
^{40}Ar	^{41}Ar	2491.6 ± 0.7	1197	99 %	1293	99 %
			814	0.0525 %	1677	0.0525 %
			2491	0.8 %	-	-
^{14}C	^{15}C	9771.7 ± 0.8	4472.88	63.2 %	5297.817	63.2 %
			9771.7	36.8 %	-	-
^{18}O	^{19}O	4821 ± 3	3266.96	54 %	1356.9	50 %
					197.1	96 %
			4623.86	45 %	197.1	96 %
^{27}Al	^{28}Al	4642.24 ± 0.14	2863.21	100 %	1778.969	100 %
^{55}Mn	^{56}Mn	3695.5 ± 0.3	735.58	14.6 %	2113.123	14.3 %
					846.771	98.9 %
			1037.94	27.9 %	1810.772	27.2 %
					846.771	98.9 %
			2848.72	56.3 %	846.771	98.9 %

effect of beta radiation should also be evaluated. In Table 2, the activated beta-emitter isotopes in Ar/CO_2 and the most significant ones of them in aluminium housing have been collected. As an example, according to the calculated activity concentrations (see Figure 4), only ^{41}Ar has a considerable activity in the counting gas. Therefore the only beta that might be taken into account is the 1197 keV ^{41}Ar beta. However, with the usual threshold settings [15] of proportional systems, the energy-deposition of the beta-radiation does not appear in the measured signal. Therefore on the one hand, the effect of beta radiation is negligible in terms of the detector signal-to-background ratio, while on the other hand, in terms of radiation protection, due to the few 10 cm absorption length in gas and few millimeters absorption length in aluminium, the beta exposure from the detector is also negligible.

Consequently only the prompt and the decay gamma emission have considerable yield to the measured background spectrum, and both of them are dominated by the ^{41}Ar, during and after the irradiation. A typical neutron beam-on gamma emission spectrum is shown in Figure 6, for 1.8 Å, 10^4 n/cm^2/s incident neutron flux, calculated with saturated ^{41}Ar activity.

In order to demonstrate how the gamma radiation background, induced by neutrons in the detector itself, affects the measured signal, signal-to-background ratio has been calculated for detector-filling gas, on the basis of Equations 5 and 6. As afore described, Ar/CO_2 can be represented with ^{41}Ar in terms of gamma emission. According to its very small saturation time, both the prompt and the decay gamma production have been considered in the background.
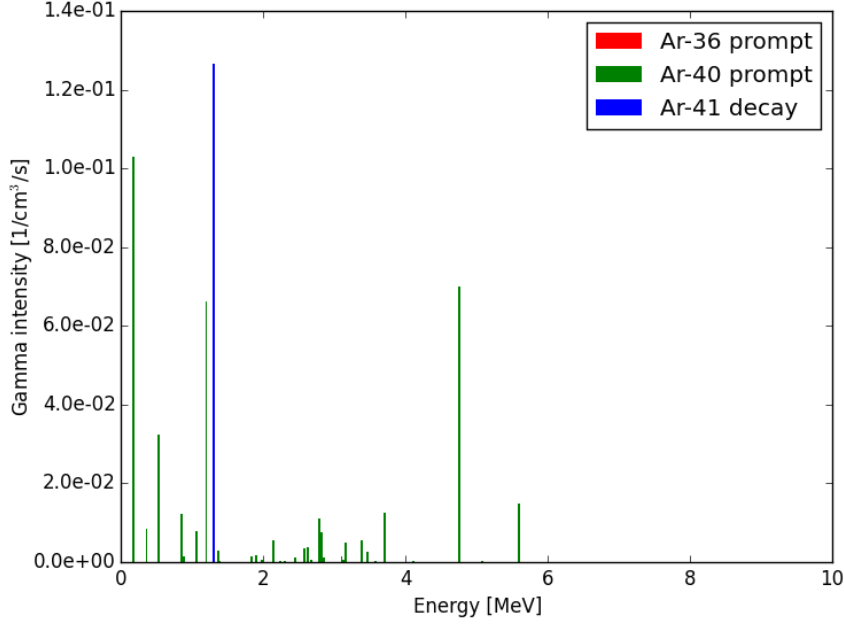
Figure 6: Overall prompt and saturated decay gamma spectrum from natural argon, irradiated with 10^4 n/cm^2/s flux of 1.8 Å neutrons. Result of calculation on the basis of reaction rates, simulated with MCNP6.1 and decay constant data from Table of Isotopes [25], as explained in text. (For interpretation of the references to color in this figure caption, the reader is referred to the web version of this article.)

In Figure 7 the good agreement of the calculated and the simulated signal-to-background ratios are shown, for the self-induced gamma background coming from neutron activation. For both cases, the signal-to-background ratio increases with the square root of the energy and varies between $10^9 - 10^{10}$ through the entire energy range. The calculation has been done with a 10^{-1} order of magnitude neutron efficiency, that is typical for a well-designed boron-carbide based neutron detector, and it has been shown that the effect of gamma background is really small, giving only a negligible contribution to the measured signal. Moreover, applying the same calculation for beam monitors, having the lowest possible neutron efficiency (approximated as 10^{-5}), the signal-to-background ratio is still 10^5, meaning that even for beam monitors the self-induced gamma
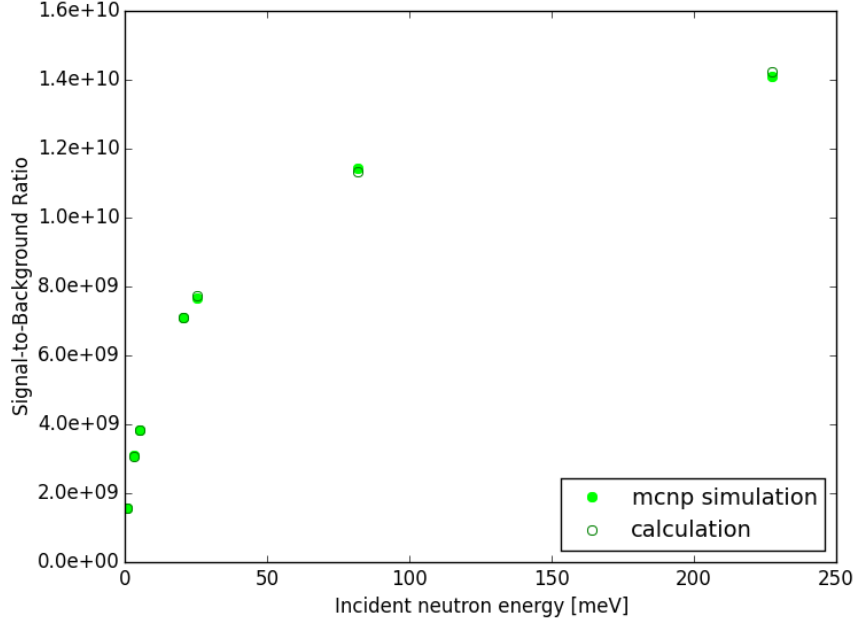
20

Figure 7: Simulated and calculated self-induced signal-to-background ratio for total gamma emission in argon, irradiated with 10^4 n/cm^2/s neutron flux. (For interpretation of the references to color in this figure caption, the reader is referred to the web version of this article.)

background is vanishingly small.

4.3. Prompt gamma intensity in Al5754 aluminium frame

The prompt and decay photon yield of the aluminium frame or housing of the detectors have been determined via analytical calculation and MCNP6.1 simulation with the same methods and parameters as the ones used for the Ar/CO$_2$. Prompt photon production normalised with incident neutron flux has been calculated.

For the Al5754 alloy as well, the calculated and MCNP6.1 simulated spectra qualitatively agree, although the agreement within the total prompt photon production varies from element to element, as shown in Table 3. Even with the best fitting choice of cross section databases (Table A4), the difference is not

higher than 10 % for most elements, but for Mn and Zn the differences between the prompt photon productions are 28 % and 23 %, respectively. However, since for all isotopes of these elements the simulation results are conservative, the MCNP simulation remains reliable. Figure 8 is given as an example to show the produced prompt photon spectrum for $\Phi = 1$ n/cm^2/s neutron flux, irradiating an 1 cm^3 volume.
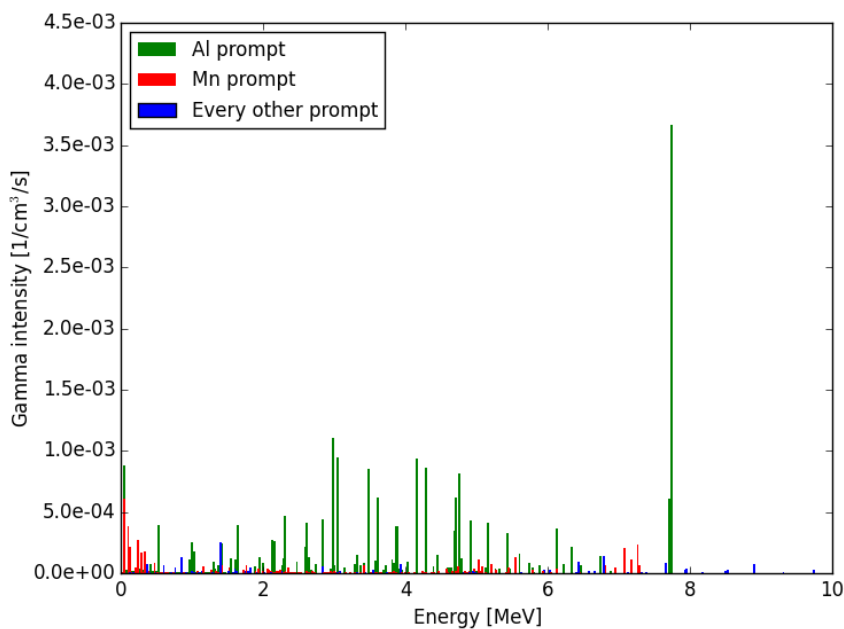

Figure 8: Prompt photon emission spectra from Al5754 aluminium alloy, irradiated with unit flux of 1.8 Å neutrons. Results of MCNP6.1 simulation, as explained in text. (For interpretation of the references to color in this figure caption, the reader is referred to the web version of this article.)

Comparing the prompt photon emission from a unit volume of Al5754 with the same for Ar/CO$_2$ (see Table 1) it can be stated, that the prompt photon intensity coming from the aluminium housing is 3 orders of magnitude higher than the one coming from the counting gas. However, for large area detectors, like the ones used in chopper spectrometry, where the gas volume might be

10^5 cm^3 (see [3–6]) the prompt photon yield of the detector counting gas can become comparable to that of the solid frame.

Table 3: Elemental composition of Al5754 [35], where m% is the mass fraction of each element in the alloy, and ΔI_{ph} is the maximum difference between calculated and simulated (MCNP6.1) total prompt photon production for all elements.

Element	m%	ΔI_{ph}
Al	97.4	10 %
Cr	0.3	5 %
Cu	0.1	9 %
Fe	0.4	5 %
Mg	3.6	6 %
Mn	0.5	28 %
Si	0.4	10 %
Ti	0.15	10 %
Zn	0.2	23 %

The two main contributors to the prompt photon emission are the aluminium and the manganese (Figure 9); the aluminium total prompt photon yield is 2 order of magnitudes, while the manganese total prompt photon yield is 1 order of magnitude higher than the yield of the rest, respectively. Consequently, even the minor components in the aluminium alloy can be relevant for photon production, if they are having a considerable neutron capture cross section. According to Figure 8, within the simulated Al5754 prompt gamma spectrum, there is one main gamma line that is responsible for the majority of the emission, 7724.03 ± 0.04 keV line of ^{27}Al. It has to be mentioned, that in the analytically calculated spectrum a second main gamma line appears at 30.638 ± 0.001 keV, also from ^{27}Al; it only has a significant yield on the basis of IAEA Data, that is not reproduced within the simulation. However, the mentioned gamma energy is low enough that for practical purposes the MCNP simulation remains reliable.
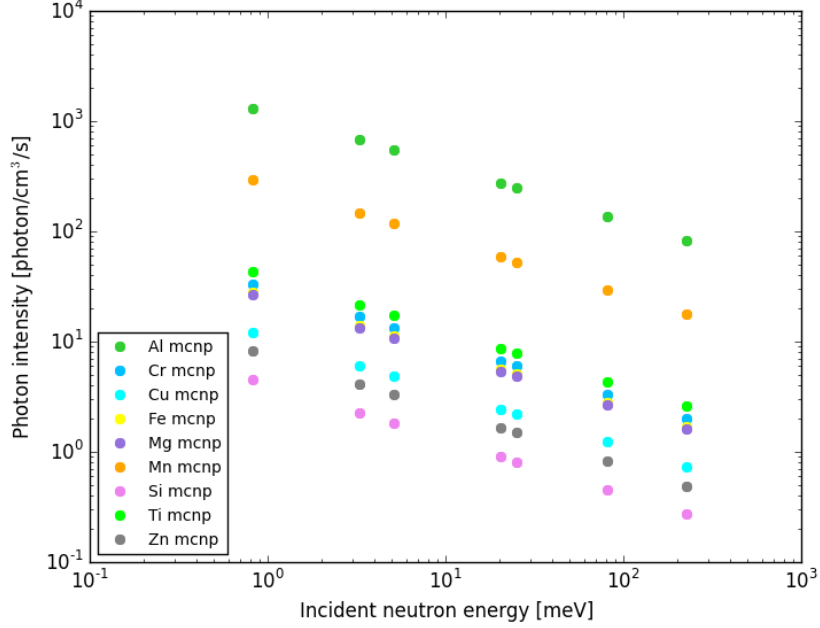
Figure 9: Elemental distribution of total prompt photon intensity in Al5754 aluminium alloy, irradiated with 10^4 n/cm^2/s flux of neutrons. Results of MCNP6.1 simulation, as explained in text. (For interpretation of the references to color in this figure caption, the reader is referred to the web version of this article.)

4.4. Activity concentration and decay gammas in Al5754 aluminium frame

An analytical calculation has been performed in order to determine the induced activity in the irradiated aluminium housing, as well as the photon yield coming from the activated radionuclides, with the same methods that have been used for the counting gas. The calculation was based on the bibliographical thermal neutron capture cross sections and the half-lives of the isotopes in the AL5754 aluminium alloy (see Table A3).

An example of the activity build-up during irradiation time for 1.8 Å is presented in Figure 10 for all the produced radionuclei. According to Figures 10 and 12, for most of the isotopes in Al5754 the activity concentrations obtained from calculations and MCNP6.1 simulations agree within the margin of error or

24

within the range of 5 %. However, for a few isotopes the difference is significant. In the case of ^{55}Cr with the most suitable choice of cross section libraries largest discrepancy between the simulations and the calculations [44] is 13 %. Also extra care is needed when treating Zn in the simulations; with calculations made on the basis of the thermal neutron cross section data of Mughabghab [44], the discrepancies for ^{65}Zn, ^{69}Zn, ^{71}Zn are 5 %, 7 % and 10 % respectively, while in the case of using the NIST database [45] for the calculations, the differences were 18 %, 3 % and 1 %. Since ^{64}Zn, the parent isotope of ^{65}Zn is the major component in the natural zinc, the usage of the first database is recommended. According to Table 1, the activity concentration of the zinc is 5 orders of magnitude smaller than the highest occurring activity concentration, hence the large difference between the calculated and the simulated result does not have a significant impact on the results of the whole alloy.

In Figure 10 it is demonstrated, that the majority of the produced total activity is estimated to be given by the ^{28}Al and the ^{55}Mn, $1.33 \cdot 10^2$ Bq/cm^3 and $1.96 \cdot 10^1$ Bq/cm^3 at the end of the irradiation time, respectively. It is also shown, that for all isotopes the activity concentration saturates quickly at the beginning of the irradiation time, therefore the decay gamma radiation is also produced practically during the entire irradiation time, with a yield constant in time.

The decay gamma intensity of the activated radionuclei from a unit volume has also been calculated, with the activity reached by the end of the irradiation time, like in case of Ar/CO$_2$ (see Table 1). It is shown that the decay gamma given by the ^{28}Al and ^{55}Mn; their decay photon emission is 3 and 2 orders of magnitude higher then the rest. The decay gamma spectrum is dominated by the 1778.969 ± 0.012 keV line of ^{28}Al.

Figure 9 and Table 1 demonstrate, that for aluminium and manganese the prompt photon production ($2.47 \cdot 10^2$ and $5.27 \cdot 10^1$ $\frac{\text{photon/cm}^3/\text{s}}{\text{n/cm}^2/\text{s}}$) and the saturated decay gamma production ($1.33 \cdot 10^2$ and $2.8 \cdot 10^1$ $\frac{\text{photon/cm}^3/\text{s}}{\text{n/cm}^2/\text{s}}$) are comparable; the yield of decay photon is 53-54 % of that of the prompt photon one, whereas for all the other isotopes the decay gamma production is less than 1 %
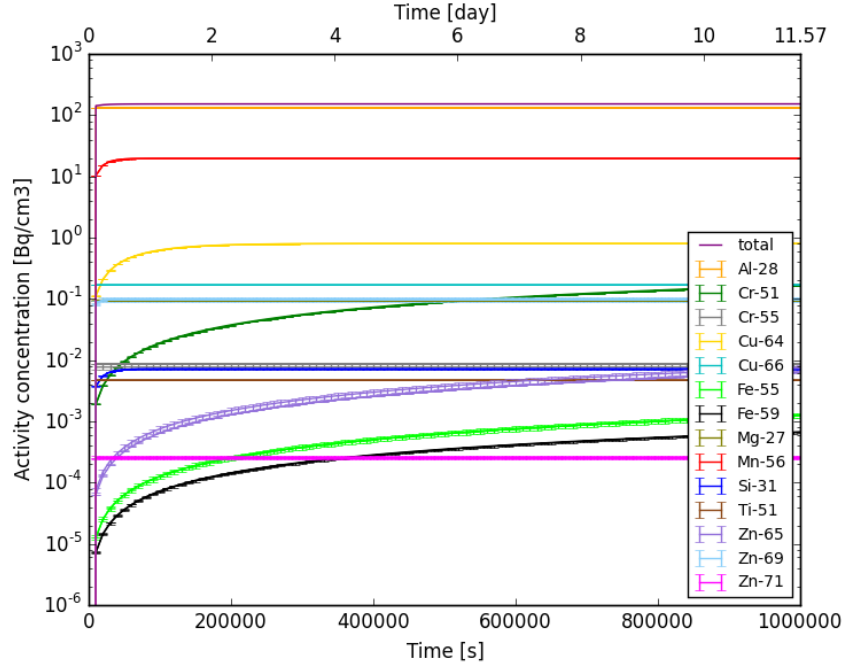
25

Figure 10: Build-up of isotopic and total activity concentration [Bq/cm^3] in Al5754 aluminium alloy during a 10^6 s irradiation time. Results of MCNP6.1 simulation and analytical calculations [25; 44], as explained in text. (For interpretation of the references to color in this figure caption, the reader is referred to the web version of this article.)

compared to the prompt gamma production.

Figure 11 depicts that the total gamma emission spectrum during the neutron irradiation is dominated by the aluminium. The majority of the total photon yield comes from the ^{27}Al prompt gamma emission, while the two main lines of the measured spectrum are the 1778.969 ± 0.012 keV ^{28}Al decay gamma and the 7724.03 ± 0.04 keV ^{27}Al prompt gamma line.

The decrease of activity in the detector counting gas because of the natural radioactive decay has also been calculated and the obtained results are shown in Figure 12, like in the case of Ar/CO$_2$ in Figure 5. There are three isotopes that become major components of the total activity for some period during the cooling time: ^{28}Al with 1 order of magnitude higher activity than the rest within
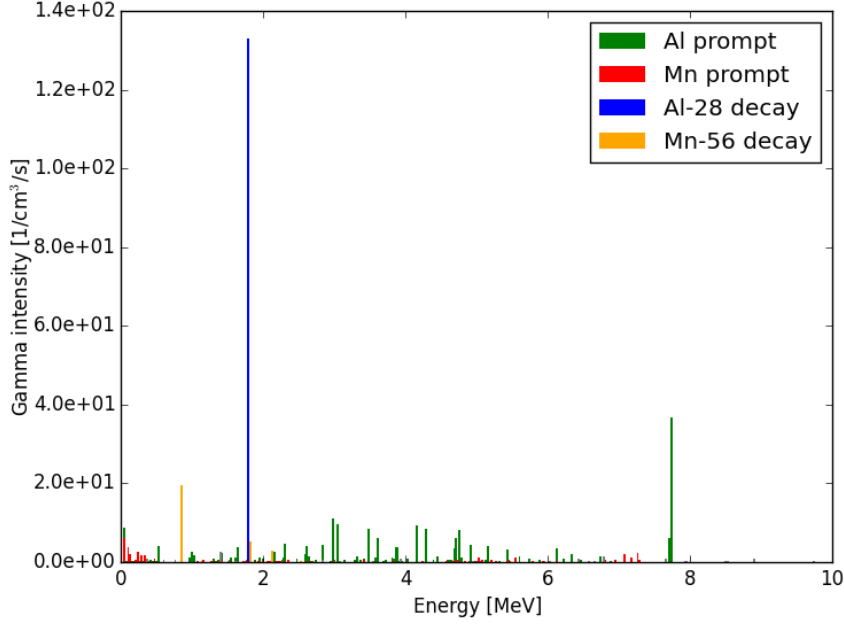
Figure 11: Overall prompt and saturated decay gamma spectrum from Al5754 aluminium alloy, irradiated with 10^4 n/cm^2/s flux of 1.8 Å neutrons. Result of calculation on the basis of reaction rates, simulated with MCNP6.1 and decay constant data from Table of Isotopes [25], as explained in text. (For interpretation of the references to color in this figure caption, the reader is referred to the web version of this article.)

0-6·10^3 s (10 min), ^{56}Mn with 2 orders of magnitude higher activity than the rest within 6·10^3-10^6 s (11 days), and ^{51}Cr with 1 order of magnitude higher activity than the rest from 10^6 s, therefore the total activity decrease is relatively fast. However, because of the long half-life of ^{55}Fe, ($T_{\frac{1}{2}} = 2.73 \pm 0.03$ y), a small backround activity is expected to remain for years after the irradiation.

5. Conclusions

Analytical calculations and MCNP6.1 modelling have been prepared and compared in order to study the effect of neutron activation in boron-carbide-based neutron detectors. A set of MCNP6.1 cross section databases has been
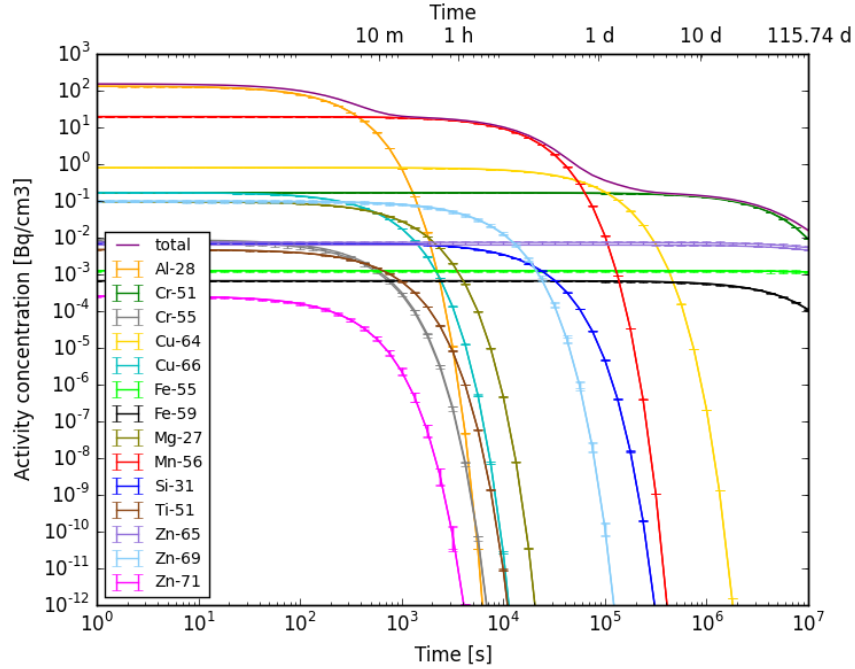
Figure 12: Decrease of activity concentration [Bq/cm^3] in Al5754 aluminium alloy from end of the 10^6 s irradiation period. Results of MCNP6.1 simulation and analytical calculations [25; 44], as explained in text. (For interpretation of the references to color in this figure caption, the reader is referred to the web version of this article.)

collected for Ar/CO_2 counting gas and aluminium detector housing estimated as Al5754, which both give good agreement with the analytical calculations, or give an acceptable, conservative estimation both for prompt gamma production and activity calculations. These databases are recommended to use for more complex geometries, where the analytical calculations should be replaced by MCNP simulations.

It has been shown, that the prompt photon emission of the aluminium housing is dominated by the Al and Mn contributors, while that of the counting gas is mainly given by Ar. The prompt photon intensity from an aluminium-housing unit volume is 3 orders of magnitude higher than from that of the counting gas.

The total activity concentration of the housing is mainly given by the ^{28}Al

and the ^{56}Mn, and given by the ^{41}Ar in the counting gas. Due to the short half-lives of the main isotopes, their decay gammas already appear and saturate during the irradiation period, giving a comparable decay gamma emission to the prompt photon emission in terms of yield.

With the afore mentioned typical counting gas, the decay gamma yield of ^{41}Ar saturates at $1.28 \cdot 10^{-1} Bq/cm^3$, and based on this value, operational scenarios can be envisaged. With these results it has been shown, that only a low level of activation is expected in the detector counting gas. Therefore with a flushing of 1 detector volume of gas per day, assuming a $V = 10^7$ cm^3 detector volume, $1.28 \cdot 10^6$ Bq/day activity production is expected. By varying the flush rate and storing the counting gas up to 1 day before release, only negligible levels of activity will be present in the waste Ar/CO_2 stream.

Neutron-induced gamma signal-to-background ratio has also been determined for several neutron energies, revealing that the signal-to-background ratio changes within the range of $10^9 - 10^{10}$ for general boron-carbide-based detector geometries, and still being 10^5 even for beam monitors, having the lowest possible efficiency.

The effect of beta-radiation coming from the activated isotopes has also been considered, and it can be stated that the beta-radiation is negligible both in terms of the signal-to-background ratio and in terms of radiation protection.

In this study all simulations and calculations were made for a generic geometry, and a reliable set of data on activity and photon production were given that can be generally applied and scaled for any kind or boron-carbide-based neutron detector, filled with Ar/CO_2.

Acknowledgments

Appendix

Table A1: (n,γ) reaction cross sections at 25.30 meV [44], reaction products, their decay constants and respective uncertainties [25] ($\sigma(^{14}C)$ is from TENDL-2014 database [37]).

Isotope	Reaction product	σ [barn]	$\Delta\sigma$ [barn]	λ [s^{-1}]	$\Delta\lambda$ [s^{-1}]
^{36}Ar	^{37}Ar	$5.20 \cdot 10^{0}$	$5.00 \cdot 10^{-1}$	$2.29 \cdot 10^{-7}$	$2.61 \cdot 10^{-10}$
^{38}Ar	^{39}Ar	$8.00 \cdot 10^{-1}$	$2.00 \cdot 10^{-1}$	$8.17 \cdot 10^{-11}$	$9.11 \cdot 10^{-13}$
^{40}Ar	^{41}Ar	$6.60 \cdot 10^{-1}$	$1.00 \cdot 10^{-2}$	$1.06 \cdot 10^{-4}$	$1.16 \cdot 10^{-7}$
^{16}O	^{17}O	$1.90 \cdot 10^{-4}$	$1.90 \cdot 10^{-5}$	stable	-
^{17}O	^{18}O	$5.38 \cdot 10^{-4}$	$6.50 \cdot 10^{-5}$	stable	-
^{18}O	^{19}O	$1.60 \cdot 10^{-4}$	$1.00 \cdot 10^{-5}$	$2.58 \cdot 10^{-2}$	$7.66 \cdot 10^{-5}$
^{12}C	^{13}C	$3.53 \cdot 10^{-3}$	$2.00 \cdot 10^{-3}$	stable	-
^{13}C	^{14}C	$1.37 \cdot 10^{-3}$	$4.00 \cdot 10^{-5}$	$3.84 \cdot 10^{-12}$	$2.67 \cdot 10^{-14}$
^{14}C	^{15}C	$8.11 \cdot 10^{-7}$	-	$2.83 \cdot 10^{-1}$	$5.78 \cdot 10^{-4}$

Table A2: Cross section for Ar/CO$_2$ libraries used in MCNP6.1 simulations [41].

Element	Prompt gamma production		(n,γ) reaction rate calculation	
Ar	18000.42c	LANL	18036.80c	ENDF/B-VII.1
			18038.80c	ENDF/B-VII.1
			18040.80c	ENDF/B-VII.1
C	6000.80c	ENDF/B-VII.1	6012.00c	TALYS-2015
			6013.00c	TALYS-2015
			6014.00c	TALYS-2015
O	8000.80c	ENDF/B-VII.1	8016.00c	TALYS-2015
			8017.00c	TALYS-2015
			8018.00c	TALYS-2015

Table A3: (n,γ) reaction cross sections at 25.30 meV [44], reaction products, their decay constants and respective uncertainties [25].

Isotope	Reaction product	σ [barn]	$\Delta\sigma$ [barn]	λ [s^{-1}]	$\Delta\lambda$ [s^{-1}]
^{27}Al	^{28}Al	$2.31 \cdot 10^{-1}$	$3.00 \cdot 10^{-3}$	$1.35 \cdot 10^{2}$	$7.20 \cdot 10^{-2}$
^{50}Cr	^{51}Cr	$1.59 \cdot 10^{1}$	$2.00 \cdot 10^{-1}$	$2.39 \cdot 10^{6}$	$2.07 \cdot 10^{2}$
^{52}Cr	^{53}Cr	$7.60 \cdot 10^{-1}$	$6.00 \cdot 10^{-2}$	stable	-
^{53}Cr	^{54}Cr	$1.82 \cdot 10^{1}$	$1.50 \cdot 10^{0}$	stable	-
^{54}Cr	^{55}Cr	$3.60 \cdot 10^{-1}$	$4.00 \cdot 10^{-2}$	$2.10 \cdot 10^{2}$	$1.80 \cdot 10^{-1}$
^{63}Cu	^{64}Cu	$4.50 \cdot 10^{0}$	$2.00 \cdot 10^{-2}$	$4.57 \cdot 10^{4}$	$7.20 \cdot 10^{0}$
^{65}Cu	^{66}Cu	$2.17 \cdot 10^{0}$	$3.00 \cdot 10^{-2}$	$3.07 \cdot 10^{2}$	$8.40 \cdot 10^{-1}$
^{54}Fe	^{55}Fe	$2.25 \cdot 10^{0}$	$1.80 \cdot 10^{-1}$	$8.61 \cdot 10^{7}$	$9.46 \cdot 10^{5}$
^{56}Fe	^{57}Fe	$2.59 \cdot 10^{0}$	$1.40 \cdot 10^{-1}$	stable	-
^{57}Fe	^{58}Fe	$2.48 \cdot 10^{0}$	$3.00 \cdot 10^{-1}$	stable	-
^{58}Fe	^{59}Fe	$1.28 \cdot 10^{0}$	$5.00 \cdot 10^{-2}$	$3.85 \cdot 10^{6}$	$5.18 \cdot 10^{2}$
^{24}Mg	^{25}Mg	$5.10 \cdot 10^{-2}$	$5.00 \cdot 10^{-3}$	stable	-
^{25}Mg	^{26}Mg	$1.90 \cdot 10^{-1}$	$3.00 \cdot 10^{-2}$	stable	-
^{26}Mg	^{27}Mg	$3.82 \cdot 10^{-2}$	$8.00 \cdot 10^{-4}$	$5.67 \cdot 10^{2}$	$7.20 \cdot 10^{-1}$
^{55}Mn	^{56}Mn	$1.33 \cdot 10^{1}$	$2.00 \cdot 10^{-1}$	$9.28 \cdot 10^{3}$	$7.20 \cdot 10^{-1}$
^{28}Si	^{29}Si	$1.77 \cdot 10^{-1}$	$5.00 \cdot 10^{-3}$	stable	-
^{29}Si	^{30}Si	$1.01 \cdot 10^{-1}$	$1.40 \cdot 10^{-2}$	stable	-
^{30}Si	^{31}Si	$1.07 \cdot 10^{-1}$	$2.00 \cdot 10^{-3}$	$9.44 \cdot 10^{3}$	$1.80 \cdot 10^{2}$
^{46}Ti	^{47}Ti	$5.90 \cdot 10^{-1}$	$1.80 \cdot 10^{-1}$	stable	-
^{47}Ti	^{48}Ti	$1.70 \cdot 10^{0}$	$2.00 \cdot 10^{-1}$	stable	-
^{48}Ti	^{49}Ti	$7.84 \cdot 10^{0}$	$2.50 \cdot 10^{-1}$	stable	-
^{49}Ti	^{50}Ti	$2.20 \cdot 10^{0}$	$3.00 \cdot 10^{-1}$	stable	-
^{50}Ti	^{51}Ti	$1.79 \cdot 10^{-1}$	$3.00 \cdot 10^{-1}$	$3.46 \cdot 10^{2}$	$6.00 \cdot 10^{-1}$
^{64}Zn	^{65}Zn	$7.60 \cdot 10^{-1}$	$2.00 \cdot 10^{-2}$	$2.11 \cdot 10^{7}$	$2.25 \cdot 10^{4}$
^{66}Zn	^{67}Zn	$8.50 \cdot 10^{-1}$	$2.00 \cdot 10^{-1}$	stable	-
^{67}Zn	^{68}Zn	$6.80 \cdot 10^{0}$	$8.00 \cdot 10^{-1}$	stable	-
^{68}Zn	^{69}Zn	$1.00 \cdot 10^{1}$	$1.00 \cdot 10^{-1}$	$3.38 \cdot 10^{3}$	$5.40 \cdot 10^{1}$
^{70}Zn	^{71}Zn	$8.30 \cdot 10^{-2}$	$5.00 \cdot 10^{-3}$	$1.47 \cdot 10^{2}$	$6.00 \cdot 10^{0}$

Table A4: Cross section libraries for Al5754 used in MCNP6.1 simulations [41].

Element	Prompt gamma production		(n,γ) reaction rate calculation	
Al	13027.66c	ENDF/B-VI.6	13027.80c	ENDF/B-VII.1
Cr	24050.80c	ENDF/B-VII.1	24050.80c	ENDF/B-VII.1
	24052.80c	ENDF/B-VII.1	24052.80c	ENDF/B-VII.1
	24053.80c	ENDF/B-VII.1	24053.80c	ENDF/B-VII.1
	24054.80c	ENDF/B-VII.1	24054.80c	ENDF/B-VII.1
Cu	29063.80c	ENDF/B-VII.1	29063.80c	ENDF/B-VII.1
	29065.80c	ENDF/B-VII.1	29065.80c	ENDF/B-VII.1
Fe	26054.80c	ENDF/B-VII.1	26054.00c	TALYS-2015
	26056.80c	ENDF/B-VII.1	26056.00c	TALYS-2015
	26057.80c	ENDF/B-VII.1	26057.00c	TALYS-2015
	26058.80c	ENDF/B-VII.1	26058.00c	TALYS-2015
Mg	12000.62c	ENDF/B-VI.8	12024.80c	ENDF/B-VII.1
			12025.80c	ENDF/B-VII.1
			12026.80c	ENDF/B-VII.1
Mn	25055.62c	ENDF/B-VI.8	25055.80c	ENDF/B-VII.1
Si	14000.60c	ENDF/B-VI.0	14028.80c	ENDF/B-VII.1
			14029.80c	ENDF/B-VII.1
			14030.80c	ENDF/B-VII.1
Ti	22000.62c	ENDF/B-VI.8	22046.80c	ENDF/B-VII.1
			22047.80c	ENDF/B-VII.1
			22048.80c	ENDF/B-VII.1
			22049.80c	ENDF/B-VII.1
			22050.80c	ENDF/B-VII.1
Zn	30064.80c	ENDF/B-VII.1	30064.00c	TALYS-2015
	30066.80c	ENDF/B-VII.1	30066.00c	TALYS-2015
	30067.80c	ENDF/B-VII.1	30067.00c	TALYS-2015
	30068.80c	ENDF/B-VII.1	30068.00c	TALYS-2015
	30070.80c	ENDF/B-VII.1	30070.00c	TALYS-2015

References

[1] European Spallation Source ESS ERIC.
URL http://europeanspallationsource.se/

[2] ESS Technical Design Report (ESS-2014-0001).
URL http://eval.esss.lu.se/cgi-bin/public/DocDB/ShowDocument?docid=274

[3] P. P. Deen, A. Vickery, ESS Instrument Construction Proposal VOR: Versatile, Optimal Resolution Chopper Spectrometer.
URL https://europeanspallationsource.se/sites/default/files/vor_2014_march.pdf

[4] P. P. Deen, A. Vickery, K. H. Andersen, R. Hall-Wilton, A design study of VOR: a Versatile Optimal Resolution chopper spectrometer for the ESS, EPJ Web of Conferences 83 (03002).

[5] W. Lohstroh, W. Petry, J. Neuhaus, L. Silvi, C. Alba-Simionesco, J.-M. Zanotti, S. Longeville, ESS Instrument Construction Proposal C-SPEC - Cold chopper spectrometer.
URL https://europeanspallationsource.se/sites/default/files/c-spec_proposal_0.pdf

[6] T. Brückel, J. Voigt, N. Violini, A. Orecchini, A. Paciaroni, F. Sacchetti, M. Zanatt, ESS Instrument Construction Proposal T-REX: A Time-of-flight Reciprocal space Explorer.
URL https://europeanspallationsource.se/sites/default/files/t-rex_proposal.pdf

[7] D. Bódis, Atommagsugárzások méréstechnikái, TYPOTEX, 2009.

[8] G. Knoll, Radiation Detection and Measurement, 4th Edition, JohnWiley & Sons, Inc., 2010, Ch. 5-6, pp. 131–207.

[9] F. Sauli, Principles of operation of multiwire proportional and drift chambers, CERN 77-09 (1977).

[10] C. Höglund, B4C thin films for neutron detection, J. Appl. Phys. 111 (2012) (104908).

[11] K. Andersen, et al., 10B multi-grid proportional gas counters for large area thermal neutron detectors, Nucl. Instr. and Meth. A 720 (2013) 116–121.

[12] F. Piscitelli, J. C. Buffet, J. F. Clergeau, S. Cuccaro, B. Guérard, A. Khaplanov, Q. La Manna, J. M. Rigal, P. Van Esch, Study of a high spatial resolution 10B-based thermal neutron detector for application in neutron reflectometry: the Multi-Blade prototype, JINST 9 (2014) (P03007).

[13] I. Stefanescu, Y. Abdullahi, J. Birch, I. Defendi, R. Hall-Wilton, C. Höglund, L. Hultman, M. Zee, K. Zeitelhack, A 10B-based neuron detector with stacked multiwire proportional counters and macrostructured cathodes, JINST 8 (2013) (P12003).

[14] G. Nowak, et al., Boron carbide coatings for neutron detection probed by x-rays, ions, and neutrons to determine thin film quality, Journal of Applied Physics 117 (2015) 034901.

[15] F. Piscitelli, P. Van Esch, Analytical modeling of thin film neutron converters and its application to thermal neutron gas detectors, JINST 8 (2013) P04020.

[16] N. Cherkashyna, et al., Overcoming High Energy Backgrounds at Pulsed Spallation Sources, arXiv:1501.02364 [physics.ins-det] (2014).

[17] B. J. Jun, et al., Estimation of aluminium and argon activation sources in the HANARO coolant, Nuclear Engineering and Technology (2014) Vol. 42 (2).

[18] M. Hoq, et al., Estimation of ^{41}Ar activity and release rate from the TRIGA MARK-II research reactor, Journal of Environmental Radioactivity 153 (2016) 68–72.

[19] C. Rojas-Palma, et al., Experimental evaluation of gamma fluence-rate predictions from argon-41 releases to the atmosphere over a nuclear research reactor site, Radiation Protection Dosimetry Vol. 108 (2) (2004) 161–168.

[20] B. Lauritzen, et al., Atmospheric dispersion or argon-41 from nuclear research reactor: measurement and modelling of plume geometry and gamma radiation field, Int. J. of Environmental and Pollution 20 (1-6) (2013) 47–54.

[21] J. Kunst, et al., Mediciones de Ar-41 y la preparaciónpara emergencias nucleares, in: VIII Congresso Regiónal de Seguridad Radiologica y Nuclear, Congreso Latinoamericano del IRPA y el V Congreso Nacional de Protección Radiolgica DSSA., 11 al 15 de octubre de 2010., Medellín, Colombia, 2010.

[22] Production and atmospheric release of activation products, in: Savannah River Site Environmental Dose Reconstruction Project; Phase II: Source Term Calculation and Ingestion Pathway Data Retrieval; Evaluation of Materials Released from the Savannah River Site, 2012, Ch. 4.3.

[23] M. McDonald, F. Ghanbari, M. Burger, C. Holm, Radioactive air effluent emission measurements at two research reactors, UNT Digital Library.
URL http://digital.library.unt.edu/ark:/67531/metadc678287/.

[24] T. Chandrasekaran, J. Y. Lee, C. A. Willis, Calculation of releases of radioactive materials in gaseous and liquid effluents from pressurized water reactors: Pwr-gale code (nureg-0017, revision 1), Division of Systems Integration, Office of Nuclear Reactor Regulation, U.S. Nuclear Regulatory Commission, Washington, DC 20555-0001 (April 1985).

[25] The Lund/LBNL nuclear data search.
URL http://nucleardata.nuclear.lu.se/toi/

[26] COUNCIL DIRECTIVE 2013/59/EURATOM, 2013.

[27] Radiological Safety Review of Siting Aspects of the ESS Technical Design Report, Tech. rep.

[28] D. Ene, M. Brandin, M. Eshraqi, M. Lindroos, S. Peggs, H. Hahn, Radiation Protection Studies for ESS Superconducing Linear Accelerator, Progress in NUCLEAR SCIENCE and TECHNOLOGY Vol. 2 (2011) 382–388.

[29] K. G. Andersson, S. P. Nielsen, External doses from the most important potential contaminants from routine airborne releases at ESS, Tech. Rep. SSM-2012-131-83, European Spallation Source ESS AB and DTU Nutech, Technical University of Denmark (2012).

[30] A. Vértes, S. Nagy, Z. Klencsár, Handbook of Nuclear Chemistry. Volume 3: Chemical Applications of Nuclear Reactions and Radiations, 1st Edition, Vol. 3, Kluwer Academic Publisher, 2003.

[31] A. Simonits, F. D. Corte, J. Hoste, Single-Comparator Methods in Reactor Neutron Activation Analysis, Journal of Radioanalytical Chemistry Vol. 24 (1975) 31–46.

[32] F. D. Corte, A. Simonits, A. D. Wispelaere, A. Elek, k_0-Measurements and Related Nuclear Data Compilation for (n, gamma) Reactor Neutron Activation Analysis, Journal of Radioanalytical and Nuclear Chemistry Vol. 133 (No. 1) (1989) 43–130.

[33] G. L. Molnár, Handbook of Prompt Gamma Activation Analysis: with Neutron Beams, 1st Edition, Kluwer Academic Publisher, 2004.

[34] Database for Prompt Gamma-ray Neutron Activation Analysis.
URL https://www-nds.iaea.org/pgaa

[35] MakeItFrom.com, 5754 aluminium.
URL https://www.makeitfrom.com/material-properties/5754-AlMg3-3.3535-A95754-Aluminum/

[36] Reference neutron activation library, Tech. Rep. IAEA-TECDOC-1285, IAEA (2002).

[37] Evaluated nuclear data file.
URL https://www-nds.iaea.org/exfor/endf.htm

[38] C. Höglund, et al., Stability of $^{10}B_4C$ thin films under neutron radiation, Radiation Physics and Chemistry 113 (2015) 14–19.

[39] Los Alamos National Security, LLC., MCNP6 ^{TM} USER'S MANUAL, version 1.0 Edition (May 2013).

[40] TALYS.
URL http://www.talys.eu/

[41] J. L. Conlin, D. K. Parsons, M. G. Gardiner, S. J. Gray, A. C. I. Kahler, M. C. White, M. B. Lee, Listing of Available ACE Data Tables, Los Alamos National Security, LLC., rev 4 Edition.

[42] A. Khaplanov, et al., In-beam test of the Boron-10 multi-grid neutron detector at the IN6 time-of-flight spectrometer at the ILL, J. Phys.: Conf. Ser. 528 (2014) (012040).

[43] A. Khaplanov, et al., Investigation of gamma-ray sensitivity of neutron detectors based on thin converter films, JINST 8 (2013) (P10025).

[44] S. F. Mughabghab, M. Divadeenam, N. E. Holden, Neutron resonance parameters and thermal cross sections Vol. 1 (1981).

[45] Nist neutron scattering lengths and cross sections.
URL https://www.ncnr.nist.gov/resources/n-lengths/